Memory CD4+ T cells are generated in the human fetal intestine

Na Li[1], **Vincent van Unen**[1], **Tamim Abdelaal**[2,3], **Nannan Guo**[1], **Sofya A. Kasatskaya**[4,5], **Kristin Ladell**[6], **James E. McLaren**[6], **Evgeny S. Egorov**[4], **Mark Izraelson**[4], **Susana M. Chuva de Sousa Lopes**[7], **Thomas Höllt**[2,8], **Olga V Britanova**[4], **Jeroen Eggermont**[9], **Noel F.C.C. de Miranda**[10], **Dmitriy M. Chudakov**[4,5,11,12,13,14], **David A. Price**[6,15], **Boudewijn P.F. Lelieveldt**[3,9], and **Frits Koning**[1,*]

[1]Department of Immunohematology and Blood Transfusion, Leiden University Medical Center, Leiden, Netherlands [2]Leiden Computational Biology Center, Leiden University Medical Center, Leiden, Netherlands [3]Department of Pattern Recognition and Bioinformatics Group, Delft University of Technology, Delft, Netherlands [4]Shemyakin-Ovchinnikov Institute of Bioorganic Chemistry, Russian Academy of Sciences, Moscow, Russia [5]Centre for Data-Intensive Biomedicine and Biotechnology, Skolkovo Institute of Science and Technology, Moscow, Russia [6]Division of Infection and Immunity, Cardiff University School of Medicine, Cardiff, UK [7]Department of Anatomy and Embryology, Leiden University Medical Center, Leiden, Netherlands [8]Computer Graphics and Visualization Group, Delft University of Technology, Delft, Netherlands [9]Department of Radiology, Leiden University Medical Center, Leiden, Netherlands [10]Department of Pathology, Leiden University Medical Center, Leiden, Netherlands [11]Central European Institute of Technology, Masaryk University, Brno, Czech Republic [12]Department of Molecular Technologies, Pirogov Russian National Research Medical University, Moscow, Russia [13]MiLaboratory LLC, Skolkovo Innovation Centre, Moscow, Russia [14]Privolzhsky Research Medical University, Nizhny Novgorod, Russia [15]Systems Immunity Research Institute, Cardiff University School of Medicine, Cardiff, UK

*Correspondence: Frits Koning; F.Koning@lumc.nl.

Reporting Summary

Further information on research design is available in the Nature Research Life Sciences Reporting Summary linked to this article.

Data availability

Mass cytometry data are available via Flow Repository (https://flowrepository.org/id/FR-FCM-ZYRD). scRNA-seq data are available via Gene Expression Omnibus accession code GSE122846. The remaining data that support the findings of this study are available from the corresponding author upon reasonable request.

Accessions

Gene Expression Omnibus
GSE122846

ORCID: Frits Koning: 0000-0002-4007-5715

Abstract

The fetus is thought to be protected from exposure to foreign antigens, yet CD45RO^{+} T cells reside in the fetal intestine. Here we combined functional assays with mass cytometry, single-cell RNA-sequencing and high-throughput T cell antigen receptor (TCR) sequencing to characterize the CD4^{+} T cell compartment in the human fetal intestine. We identified 22 CD4^{+} T cell clusters, including naive-like, regulatory-like and memory-like subpopulations, which were confirmed and further characterized at the transcriptional level. Memory-like CD4^{+} T cells had high expression of Ki-67, indicative of cell division, and CD5, a surrogate marker of TCR avidity, and produced the cytokines IFN-γ and IL-2. Pathway analysis revealed a differentiation trajectory associated with cellular activation and proinflammatory effector functions, and TCR repertoire analysis indicated clonal expansions, distinct repertoire characteristics and interconnections between subpopulations of memory-like CD4^{+} T cells. Imaging-mass cytometry indicated that memory-like CD4^{+} T cells colocalized with antigen-presenting cells. Collectively, these results provide evidence for the generation of memory-like CD4^{+} T cells in the human fetal intestine that is consistent with exposure to foreign antigens.

Adaptive immunity is founded on the selection and expansion of antigen-specific T cells from a clonally diverse pool of naive precursors1. Naive T cells recirculate among lymph nodes to survey the array of peptide epitopes bound to major histocompatibility complex (MHC) proteins on the surface of antigen-presenting cells (APCs), and functional recognition of a given peptide-MHC molecule is governed by various danger signals and specific engagement via the clonotypically expressed T cell antigen receptor (TCR). This triggers a program of differentiation and proliferation that results in the generation of effector T cells, which home to the site of the primary infection and contribute to pathogen clearance, and memory T cells, which remain in the circulation and mediate anamnestic responses to secondary infection. In the last decade, it has also become clear that tissue-resident T cells are commonly present at barrier sites, including the intestine2.

Fundamental knowledge of adaptive immunity during early life remains sparse. The infantile intestine is known to harbor clonally expanded T cells3, which were also identified in the human fetal intestine, but rarely in fetal mesenteric lymph nodes, fetal thymus or fetal spleen, suggesting compartmentalization4. In addition, a rare population of CD4^{+} T cells displaying a memory and proinflammatory phenotype has been identified in umbilical cord blood5. Although the dogma of a sterile womb has been challenged by reports of bacteria colonization in the placenta6,7, amniotic fluid8,9 and meconium10, others have questioned these results11. Here we have combined functional studies with mass cytometry, RNA-sequencing (RNA-seq) and high-throughput TCR-sequencing to perform an in-depth analysis of the fetal intestinal CD4^{+} T cell compartment. Our results provide evidence for memory formation in the human fetal intestine, consistent with *in utero* exposure to foreign antigens.

Results

Human fetal intestinal CD4^{+} T cells are phenotypically diverse

To explore the CD4^{+} T cell compartment in the human fetal intestine, we applied a mass cytometry panel comprising 35 antibodies (Supplementary Table 1) that was designed to capture the heterogeneity of the immune system to seven lamina propria samples aged 14-21 gestational weeks[12]. After data acquisition, we selected CD45^{+} immune cells (Supplementary Fig. 1a) and mined the dataset via hierarchical stochastic neighbor embedding (HSNE)[13]. At the overview level, HSNE landmarks depicted the general composition of the immune system, with clear separation of the CD4^{+} T cell lineage (Supplementary Fig. 1b). We identified 110,332 CD4^{+} T cells, with an average of 15,761 events per fetal intestine, comprising 47.9% ± 9.6% of all immune cells. We then subjected HSNE-defined CD4^{+} T cells (Supplementary Fig. 1b) to t-distributed stochastic neighbor embedding (t-SNE)[14] in Cytosplore[15] to project their marker expression profiles onto a two-dimensional graph (Fig. 1a and Supplementary Fig. 1c). CD4^{+} T cells were characterized as CD45^{+}CD3^{+}CD4^{+}CD7^{+} (Fig. 1a). Moreover, all CD4^{+} T cells were positive for the tissue-resident marker CD38 and approximately 50% of cells expressed CD161. 24.1% of the CD4^{+} T cell population co-expressed CD27, CD28, CD45RA and CCR7, indicative of a naive T cell (T_N) phenotype, whereas 64.5% expressed CD45RO, indicative of a memory T cell (T_M) phenotype (Fig. 1a,b). While all CD45RO^{+} T_M cells were CD28^{+}, differential expression of CD25, CD27, CD103, CD117, CD127, CCR6 and CCR7 was observed on these cells (Fig. 1a,b), reflecting substantial phenotypic diversity.

We next applied Gaussian mean-shift clustering to the mass cytometry data using the t-SNE coordinates of the embedded CD4^{+} T cells (Fig. 1a). Based on cell density features (Fig. 1c), this identified 22 distinct CD4^{+} T cell clusters (Fig. 1d), each defined by a unique marker expression profile. Hierarchical clustering of the heatmap revealed eight major groups (CD161^{+}CCR6^{−}CD117^{−} T_M cells, CD161^{+}CCR6^{+}CD117^{+} T_M cells, DN T_M cells, T_{reg} cells, CD161^{−}CCR7^{+} T_M cells, CD161^{−} T_N cells, CD161^{lo} T_N/T_M cells and CD161^{−}CCR7^{−} T_M cells) (Fig. 1e). High expression of CD25 and a lack of CD127 distinguished two regulatory T (T_{reg}) cell clusters, with either a CD45RA^{+} T_N or a CD45RO^{+} T_M phenotype (Fig. 1a,b,e). CD161^{+}CD4^{+} T cells branched into a CCR6^{−}CD117^{−}CD45RO^{+} T_M and a CCR6^{+}CD117^{+}CD45RO^{+} T_M cluster (Fig. 1e). Moreover, CD45RA^{+} T_N and CD45RO^{+} T_M cells were detected in both the CD161^{−} and the CD161^{lo} subpopulations. Additional diversity was observed for the expression of several activation markers, including CRTH2, HLA-DR, KLRG-1 and PD-1, the latter especially within the CD45RO^{+} T_M cell clusters (Supplementary Fig. 1c). Of note, a small population of CD4^{−}CD8a^{−}TCRγδ^{−} (DN) T_M cells clustered among CD4^{+} T cells in both the HSNE and t-SNE plots. Biaxial plots confirmed coexpression of CD45RA and CCR7 on T_N cells (Fig. 1f), whereas the CD161^{lo/−}CD45RO^{+} T_M subpopulation contained both CCR7^{+} central memory T (T_{CM}) cells and CCR7^{−} effector memory T (T_{EM}) cells (Fig. 1f). All other CD45RO^{+} T_M subpopulations harboured primarily T_{EM} cells. Quantification of cellular frequencies for the CD4^{+} T cell clusters per fetal intestine revealed highly similar compositions with all CD45RO^{+} T_M clusters detectable in all samples (Fig. 1g). In contrast, parallel analyses of CD4^{+} T cells isolated from three fetal livers and three fetal spleens from one shared and two additional fetuses

aged 16-21 gestational weeks revealed a predominance of CD45RA$^+$ T$_N$ cells (Supplementary Fig. 2a,b). These results delineated a phenotypically diverse array of human fetal intestinal CD4$^+$ T cells, most of which displayed features associated with antigen exposure.

Fetal CD4$^+$ T cells display a memory gene expression profile

We next performed single-cell RNA-seq on flow-sorted fetal intestinal CD4$^+$ cells from a lamina propria sample that was also included in the mass cytometry analysis. This yielded data for 1,804 CD4$^+$ T cells, identifying cell-specific variable expression of 2,174 genes (Methods), which were further analyzed using the Seurat computational pipeline[16]. Unsupervised clustering revealed nine transcriptionally distinct subpopulations, seven of which corresponded to CD3$^+$ T cell subsets while two displayed a gene expression profile matching *CD86$^+$HLA-DR$^+$* APCs. The corresponding gene expression profiles of the seven T cell subsets were projected onto a single graph using t-SNE (Fig. 2a), and the top 20 upregulated genes were displayed in a heatmap (Fig. 2b). Five of the seven RNA-seq-identified CD4$^+$ T cell subpopulations corresponded to the mass cytometry-defined CD4$^+$ T cell major groups: *CCR7$^+$* T$_N$ with CD45RA$^+$ T$_N$, *KLRB1$^{lo/-}$SELL$^-$* T$_M$ with CD161$^{lo/-}$CD45RO$^+$ T$_M$, *KLRB1$^+$CCR6$^-$SELL$^-$* T$_M$ with CD161$^+$CCR6$^-$CD45RO$^+$ T$_M$, *KLRB1$^+$CCR6$^+$SELL$^-$* T$_M$ with CD161$^+$CCR6$^+$CD45RO$^+$ T$_M$ and *FOXP3$^+$* T$_{reg}$ cells with CD25$^+$CD127^{lo} T$_{reg}$ cells. The mass cytometry defined CD161$^-$ and CD161^{lo} subpopulations (Fig. 1e) could not be discriminated in the RNA-seq dataset. One additional RNA-seq-identified subpopulation corresponded to proliferating cells, based on the expression of genes associated with cell division (*CCNB2, CDK1* and *MKI67*) (Fig. 2a,b).

As CD45RA and CD45RO were not detectable, we used other markers to distinguish T$_M$ from T$_N$ clusters. To compare gene or marker expression among cell clusters, we used violin plots, displaying the mode average as the thickest section (Fig. 2c-e). Consistent with the mass cytometry data, RNA-seq-defined T$_N$ cells were *KLRB1$^-$CCR7$^+$SELL$^{+/-}$* (Fig. 2c,d), the latter confirmed by flow cytometry (Fig. 2e and Supplementary Fig. 3a). In the absence of T$_M$-associated markers, *SELL$^-$* T$_M$ cell populations were identified on the basis of differential expression of *KLRB1* and *CCR6* (Fig. 2c,d). Consistent with the mass cytometry data, expression of *KIT* (CD117) was restricted primarily to *KLRB1$^+$CCR6$^+$SELL$^-$* T$_M$ cells (Supplementary Fig. 3b). Moreover, the gene expression profile of the *IL2RA$^+$IL7R^{lo}FOXP3$^+$* T$_{reg}$ cell population (Fig. 2c) corresponded to the mass cytometry-defined CD25$^+$CD127^{lo} T$_{reg}$ cells (Fig. 2d). In addition, several RNA-transcripts including *LAG3, TIGIT, CTLA4* and *TNFRSF18* (GITR) ascertained the identity of *FOXP3$^+$* T$_{reg}$ cells (Fig. 2b). Finally, the RNA-seq data revealed an undefined T$_M$ cluster that was not identified by mass cytometry, but expressed genes similar to those detected in the *KLRB1$^+$CCR6$^+$SELL$^-$* T$_M$ subpopulation, such as *CD69, CCL5* and *JAML*. Cell population frequencies identified by mass cytometry and RNA-seq were comparable with the exception of mass cytometry-defined CD25$^+$CD127^{lo} T$_{reg}$ cells and RNA-seq-defined *FOXP3$^+$* T$_{reg}$ cells (Supplementary Fig. 3c).

Compared with the *CCR7$^+$* T$_N$ population, *KLRB1$^{lo/-}$SELL$^-$* T$_M$, *KLRB1$^+$CCR6$^-$SELL$^-$* T$_M$, *KLRB1$^+$CCR6$^+$SELL$^-$* T$_M$ and undefined T$_M$ subpopulations had high expression of

the tissue-resident and activation-associated gene *CD69*, the differentiation-promoting gene *ANXA1* (Annexin A1), the chemokine-like factor *CKLF*, the cytokine *IL32*, the proliferation-associated gene *JUN* (C-Jun) and the adhesion molecule *JAML* (Fig. 3a). *CD40LG* (CD154), *TNFSF14* and *TGFB1* were specifically upregulated by $KLRB1^+CCR6^-SELL^-$ T_M, $KLRB1^+CCR6^+SELL^-$ T_M and undefined T_M clusters, while *CCL5* and *MAP3K8* kinase upregulated by $KLRB1^+CCR6^-SELL^-$ T_M and undefined T_M subpopulations. Moreover, *IL4I1* was specifically expressed by $KLRB1^+CCR6^+SELL^-$ T_M and undefined T_M cells. In addition, all fetal $SELL^-$ T_M subpopulations had high expression of the tissue-resident genes *ITGAE* (CD103) and/or *CD38* (Fig. 3a).

In agreement with the RNA-seq data, flow cytometry indicated that the activation markers CXCR3, CCR4, CD69 and CD226 were highly expressed on $CCR7^-$ T_{EM} cells (Fig. 3b). All $CD4^+$ T cells expressed CD95, with the highest expression on $CD161^+$ T_{EM} cells (Fig. 3b). Expression of CD31, a marker associated with recent thymic emigrants[17], was highest on $CD45RA^+$ T_N cells (Fig. 3b). Thus, RNA-seq confirmed the existence of distinct subpopulations of $CD4^+$ T cells and indicate that many genes associated with inflammation and tissue residency were upregulated by fetal $CD4^+$ T_M cells, consistent with antigen-driven functionality and maturation.

Computational analysis reveals a differentiation pathway of CD4⁺ T cells

We next visualized the evolution of the t-SNE computation of the mass cytometry and RNA-seq data to reveal the ordering of single cells along putative differentiation trajectories[12,15]. At the onset of the mass cytometry data computation, where cells are grouped based on major shared features, $CD25^+CD127^{lo}$ T_{reg} cells clustered separate from the other cells, whereas the other cell clusters were ordered in a linear fashion with the $CD45RA^+$ T_N cells next to the $CD161^{lo/-}CD45RO^+$ T_M cells, followed by the $CD161^+CCR6^-CD45RO^+$ T_M cells and the $CD161^+CCR6^+CD45RO^+$ T_M cells, consecutively (Fig. 4a). A similar phenotypic ordering was observed in parallel analyses of the RNA-seq data, although the $KLRB1^+CCR6^+SELL^-$ T_M subpopulation aligned differently, but remained connected with the $KLRB1^+CCR6^-SELL^-$ T_M cluster (Fig. 4b). Individual marker expression patterns at the middle of the t-SNE computation validated the ordering of the clusters and the comparability of the mass cytometry and RNA-seq data (Supplementary Fig. 4a,b). Similar patterns were identified using Diffusion map[18], VorteX[19] and principal component analysis (PCA)[20] (Supplementary Fig. 4c–f). Thus, this analysis reveals a putative differentiation pathway leading to T_M formation.

To extend our analysis of the gene expression profiles underlying this putative differentiation trajectory, we used the pseudotime algorithm in the Monocle toolkit[21,22], which calculates the ordering of individual cells based on single-cell expression profiles. Based on this analysis, $CCR7^+$ T_N cells were separated from $SELL^-$ T_M cells (Fig. 4c). When we clustered genes according to expression patterns along the pseudotime trajectory, cell-to-cell transitioning could be explained by the kinetics of 1,376 variable genes, which formed three large modules (Fig. 4d). The first module contained 540 genes associated with $CCR7^+$ T_N cells, including *SELL*, *CCR7*, *CD27* and *CD28* (Fig. 4d). The second module contained 453 genes, many of which were associated with an ongoing transcriptional program, such as

RPL21, *RPS2* and *RPLP1*. The highest activity of this transcriptional gene expression profile coincided with the transition of cells with a *CCR7*^{+} T_N phenotype into cells with a *SELL*[−] T_M phenotype (Fig. 4c,d). The third module contained 383 genes (Fig. 4d), 106 of which were associated with cellular activation and regulation of the immune system (Supplementary Fig. 5a), while 133 encoded proteins known to interact physically with each other (Supplementary Fig. 5b). In addition, 23 genes in module 3 could be assigned to cytokine or chemokine receptor pathways, including *CCL20* and its receptor *CCR6*, the interferon receptor *IFNGR1*, TNF family members and IL-1 and IL-17 receptors (Supplementary Fig. 5b). Several signaling cascades were also represented in module 3, including the MAPK, TNF, IL-17 and TCR signaling pathways (*FYN*, *LCP2*, *SOS1*, *MAP3K8* kinase, *FASL* and *TNF*) (Fig. 4d). The $T_H 17$-associated gene *RORC* was expressed in module 3 (Fig. 4d). In addition, the dynamic expression profiles of *FYN*, *FASL* and *TNF* clustered tightly with *KLRB1* (CD161) (Fig. 4d) at the point in the pseudotime trajectory where *CCR7*^{+} T_N cells were aligned next to *SELL*^{−} T_M cells (Fig. 4d). Finally, we quantified the smoothness of cell-to-cell transitioning based on gene expression changes along the trajectory, which showed that the pseudotime trajectory was most uncertain at the beginning and toward the end, but quite robust in the middle, where *CCR7*^{+} T_N cells were aligned next to *SELL*^{−} T_M cells (Fig. 4d). In sum, these results identified temporal patterns of gene expression along the single-cell trajectory that is compatible with the transition of cells displaying a T_N phenotype into cells with a T_M phenotype.

TCR analysis reveals clonal expansion of fetal CD4^{+} T cells

Surface expression of CD5 correlates with TCR avidity[23–26]. Because *CD5* gene expression was upregulated in T_M cells compared to T_N cells, we quantified CD5 expression on all identified fetal intestinal CD4^{+} T cell subsets using flow cytometry and observed that all the CD4^{+} T cell subsets expressed CD5 (Fig. 5a), but that the median fluorescence intensity (MFI) was higher in CD161^{−} T_M, CD161^{+}CD117^{−} T_M and CD161^{+}CD117^{+} T_M cells and lower in CD25^{+}CD127^{lo} T_{reg} cells and CD45RA^{+} T_N cells (Fig. 5a–c), suggesting that cells with a T_M phenotype express TCR with a higher avidity compared to T_N cells.

Next, we evaluated the TCR clonotypic architecture of flow-sorted fetal intestinal CD45RA^{+} T_N, CD45RO^{+} T_M and CD25^{+}CD127^{lo} T_{reg} subpopulations. Analysis of the TCRβ rearrangements in a single fetal intestine indicated limited overlap among the distinct subpopulations, most of which were highly polyclonal (not shown). Distinct clonotypes were expanded among CD45RO^{+} T_M cells compared to CD45RA^{+} T_N cells (Supplementary Fig. 6a). We then used a quantitative high-throughput approach for deep sequencing of TCRα and TCRβ rearrangements in all identified fetal intestinal CD4^{+} T cell subsets isolated from two additional fetal intestines (Supplementary Table 2). Post-analysis of the obtained repertoires was conducted using VDJtools[27]. As expected, all T_M subpopulations showed greater clonality compared to the T_N subpopulation (Fig. 5d,e). The averaged characteristics of CDR3 length, added N-nucleotides and physicochemical characteristics of the 5 amino acid residues located in the middle of the CDR3 loop, which are most likely to contact the peptide-MHC complex[28], also differed among all subpopulations (Fig. 5f). The latter analysis included the averaged statistical potential of the CDR3 loop with respect to epitope interactions, comprising the estimated "energy" of the interaction with a random

epitope29, the "strength" of the interaction (derivative of "energy", VDJtools27), hydrophobicity (Kidera factor 4)30,31 and "volume" (values from http://www.imgt.org/IMGTeducation/Aide-memoire/_UK/aminoacids/IMGTclasses.html). These analyses provided no evidence for clonal expansion of CD4$^+$ T cells as a function of intrinsically high TCR-avidities for self-derived peptide-MHC complexes (Fig. d-f), suggesting indirectly that antigen-specific interactions triggered clonal selection of CD4$^+$ T cells from the T_N cell pool. Analysis of V-J segment use (Jensen-Shannon divergence; Supplementary Fig. 6b) and overlaps among repertoires in terms of the weighted proportion of shared TCRβ clonotypes revealed tightly clustered technical replicates and clearly distinguished all subpopulations of CD4$^+$ T cells (Fig. 5g). At the same time, the CD161$^-$ T_M, CD161$^+$CD117$^-$ T_M and CD161$^+$CD117$^+$ T_M cells clustered similarly in each fetus, with minimum overlap with the CD45RA$^+$ T_N and CD25$^+$CD127^{lo} T_{reg} cells (Fig. 5g). Analysis of the clonal overlap of amino acid CDR3 repertoires between the same populations in the two fetal intestines revealed that the CD161$^-$ T_M, CD161$^+$CD117$^-$ T_M and CD161$^+$CD117$^+$ T_M populations displayed much stronger overlap than the CD45RA$^+$ T_N and CD25$^+$CD127^{lo} T_{reg} CD4$^+$ T cells (Supplementary Fig. 6c), which could be explained by TCR selection due to exposure to similar foreign antigens. Finally, although the majority of the TCR repertoire was specific for each population, up to 20% of the T cell clones were shared between the CD45RA$^+$ T_N and the three CD45RO$^+$ T_M cell populations (Supplementary Fig. 6d), suggesting a potential clonal relationship between CD45RA$^+$ T_N and CD45RO$^+$ T_M cells. These results indicate that avidity-based, clonotype-specific expansion of the T_N pool was associated with T_M formation and confirmed the close relationship between CD161$^-$ T_M, CD161$^+$CD117$^-$ T_M and CD161$^+$CD117$^+$ T_M cells.

Fetal CD4$^+$ T_M cells secrete proinflammatory cytokines

To determine the functional profiles of fetal intestinal CD4$^+$ T cells, we flow-sorted CD3$^+$CD4$^+$ T cells and measured expression of TNF, IL-2, IFN-γ, IL-4, granzyme B and IL-17A in CD45RA$^+$ T_N cells and CD117$^-$ and CD117$^+$ T_M cells after cross-linking CD3 and CD28. The activation marker CD154 (CD40L) was upregulated on all cells analyzed (Fig. 6a,b), indicating efficient stimulation. All three subpopulations secreted large amounts of TNF (Fig. 6a,b), but CD117$^-$ T_M cells and CD117$^+$ T_M cells displayed the highest MFIs (Supplementary Fig. 7a). Moreover, IL-2, IFN-γ, IL-4 and granzyme B were more commonly expressed in CD117$^-$ T_M and CD117$^+$ T_M cells relative to CD45RA$^+$ T_N cells (Fig. 6a,b). The majority of cytokine-producing CD4$^+$ T cells did not express Ki-67 (Supplementary Fig. 7b). Importantly, higher frequencies of IL-2$^+$IFN-γ$^+$ cells were detected in the CD117$^-$ T_M and CD117$^+$ T_M cells compared with the CD45RA$^+$ T_N population (Supplementary Fig. 7c), suggesting greater polyfunctionality. Although the T_H17-associated *RORC* gene was expressed by 1.3% of *KLRB1$^+$CCR6$^+$SELL$^-$* T_M cells (Fig. 4d), IL-17A production was undetectable in all T_M cells. Thus, fetal intestinal CD117$^-$ T_M and CD117$^+$ T_M cells deployed multiple effector functions reminiscent of classical CD4$^+$ T_M cells in response to TCR-mediated signal transduction and costimulation via CD28.

Fetal CD4+ T cells are co-localized with antigen presenting cells

The single-cell RNA-seq analysis revealed a *MKI67+* cluster of proliferating cells, together with high expression of the T_M cell-associated markers *KLRB1* (CD161) and *CD69* and low expression of the T_N cell-associated markers *CCR7* and *SELL* (CD62L) (Fig. 7a). Flow cytometry of fetal intestinal CD4+ T cells indicated the presence of Ki-67+ cells, predominantly within the CD45RO+ compartment (Fig. 7b). To assess the spatial distribution of CD4+ T cells *in situ*, we employed a panel of 15 antibodies (Supplementary Table 3) combined with a DNA stain to perform imaging-mass cytometry on tissue sections of four human fetal intestinal samples. Stains for collagen I and smooth muscle actin were used to visualize the extracellular matrix of the basement membrane, and the epithelium and lamina propria were distinguished as vimentin−E-cadherin+ and vimentin+E-cadherin−, respectively (Fig. 7c,d). Most CD4+ T cells localized to the lamina propria (Fig. 7c,d). Differential expression of CD45RA further allowed discrimination of CD45RA+ T_N (Fig. 7c,d) from CD45RA− T_M cells in the lamina propria (Fig. 7c,d). In addition, all CD4+ T cells expressed CD38, whereas only some CD4+ T cells expressed CD69 (Fig. 7d). Using a second panel comprising 10 antibodies (Supplementary Table 3), we found that CD4+ T cells frequently colocalized with CD163+HLA-DR+ APCs (Fig. 7e). Moreover, the single-cell RNA-seq analysis of fetal intestinal cells revealed two cluster of cells displaying high expression of gene transcripts encoding HLA-DR, CD74 (HLA-class II invariant chain), inhibitory molecule PD-L1 (CD274), CD80 and CD86, typically found in APCs. Moreover, these APCs expressed gene transcripts encoding CD40, consistent with an activated phenotype (Fig. 7f), whereas stimulated fetal intestinal CD4+ T cells expressed CD40L (CD154) (Fig. 6b). In addition, 25.8% of APCs had high expression of CCR7, potentially enabling migration to the mesenteric lymph nodes (Fig. 7f). Collectively, these results indicated the existence of CD4+ T_M cells in the fetal intestine, many of which colocalized in the lamina propria with activated CD163+HLA-DR+ APCs.

Discussion

Here we used mass cytometry and single-cell RNA-seq to characterize CD4+ T cells in the human fetal intestine. Mass cytometry revealed three major populations of fetal intestinal CD4+ T cells (T_N, T_M and T_{reg} cells), that could be further distinguished into eight distinct cells clusters that displayed additional heterogeneity. These cell clusters were present in seven human fetal intestines, suggesting a physiologically robust immune composition. Single-cell RNA-seq revealed the presence of seven CD4+ T cell subpopulations, five of which displayed phenotypic overlap with the mass cytometry-defined CD4+ T cell subpopulations. We used computational tools to construct putative CD4+ T cell differentiation trajectories. Using adapted t-SNE32, we obtained remarkably similar trajectories for the mass cytometry and RNA-seq data. We identified three distinct gene expression modules along the differentiation trajectory that correspond to an increase in gene translation and subsequent activation of immune related genes. In addition, high-throughput TCR sequencing indicated clonal expansions within the CD4+ T_M cell pool, consistent with the evidence for cell proliferation within the CD45RO+ T_M pool that was obtained at both the mRNA and protein level. Moreover, CD4+ T_M cells secreted higher amounts of pro-inflammatory cytokines upon TCR triggering compared to CD4+ T_N cells.

Finally, fetal intestinal $CD4^+$ T_M cells displayed a tissue-resident profile and were frequently found to colocalize with APCs in the lamina propria. Together, this suggested that clonotype-specific transcriptional programs regulated by antigen encounter underpinned the formation of $CD4^+$ T_M cells in the fetal intestine.

T cells in umbilical cord and peripheral blood obtained of infants aged 2 months were reported to display a typical $CD45RA^+$ T_N phenotype[3]. The observation herein that a large pool of $CD45RO^+$ cells with a tissue-resident profile populated the fetal intestine suggests the compartmentalization of the immune system early in life. In conjunction with the earlier finding that clonally expanded T cells were present in the fetal intestine, but virtually absent in other fetal organs[4], our results further suggest that memory formation was driven by local exposure to foreign antigens. The observation that there is a substantial overlap in the amino acid CDR3 repertoires of the memory $CD4^+$ T cells compartment in the two fetuses analyzed may indicate exposure to similar foreign antigens.

Approximately 50% of all fetal intestinal $CD4^+$ T cells were $CD161^+$ and transcriptionally distinct from their $CD161^-$ counterparts, consistent with a recent study[33]. The kinetics of *KLRB1* (CD161) expression was preceded by increased expression CD5 and coincided with increased expression of several TCR signaling genes, including *FYN*, *FASL* and *TNF*, suggesting a coordinated program of transcription. Of note, CD161 was identified as a costimulatory molecule in the context of TCR stimulation[33].

Although the mass cytometry and RNA-seq data were largely compatible, there were exceptions. For example, coexpression of *CCR6* and *KIT* among $KLRB1^+CCR6^+SELL^-$ T_M cells was not reflected in the gene expression profiles. Conversely, expression of *ITGAE* (CD103) mRNA was not reflected by protein expression. These anomalies were likely attributable to discordant gene transcription and protein expression[34] and may also relate to differences in sensitivity of the employed techniques.

The presence of a large population of T_N cells in the fetal intestine is in stark contrast to the predominace of T_M cells in the adult intestine. As the T_N cells expressed relatively high amounts of CD31, which demarcates recent thymic emigrants, our results indicate direct migration of recent thymic emigrants into the intestine[35,36]. We propose that antigen-specific priming of T_N cells takes place in the mesenteric lymph nodes followed by migration of the resulting T_M cells to the lamina propria leading to a progressive loss of T_N cells. Similarly memory formation is taking place in the $CD8^+$ T cell compartment (not shown).

Distinct subpopulations of fetal intestinal T_{reg} cells were distinguished by several markers, including high expression of CD25 and Foxp3, and a lack of CD127. In line with previous results[37], approximately 50% of these cells expressed CD45RO, while the remainder expressed CD45RA. The $CD45RA^+$ T_{reg} cells expressed TCRs with longer CDR3β loops, higher numbers of added N-nucleotides and distinct physicochemical characteristics, suggesting higher affinities for self-antigens compared to $CD45RO^+$ T_{reg} cells[38]. The presence of oligoclonal T cell expansions in fetuses with autoimmune conditions associated

with a genetic absence of T_{reg} cells indicate a key role for these cells in immune suppression *in utero*[39].

In conclusion, our study revealed a putative differentiation trajectory in the fetal intestinal CD4^{+} T cell compartment, consistent with the formation of T_M cells *in utero*, presumably as a consequence of exposure to foreign antigens. These could include non-inherited maternal HLA-molecules[40] and pathogen-derived ligands, which could be derived from amniotic fluid[8,9]. We propose that immune priming in the fetal intestine prepares the infant for the massive influx of bacteria that occurs immediately after birth, with anamnestic responses *in situ* facilitated by the colocalization of CD4^{+} T_M cells with APCs.

Methods

Sample processing and cell isolation

Fetal tissues were obtained from elective abortions with informed consent. The gestational age ranged from 14 to 22 weeks. Intestines were separated from mesentery, cut into small pieces, embedded in optimal cutting temperature compound, and snap-frozen in isopentane. The remaining intestines were used for single-cell isolation as described previously[12]. Briefly, fetal intestines were cleared of meconium, cut into fine pieces, treated with 1 mM dithiothreitol (Fluka) for 2 x 10 min (replacing buffer) at room temperature (rT), and then incubated with 1 mM ethylenediaminetetraacetic acid (Merck) for 2 x 1 h (replacing buffer) at 37 °C under rotation to separate the epithelium from the lamina propria. To obtain single-cell suspensions from the lamina propria, the intestines were rinsed with Hank's balanced salt solution (Thermo Fisher Scientific), incubated with 10 U/mL collagenase IV (Worthington) and 200 μg/mL DNAse I grade II (Roche Diagnostics) overnight at 37 °C, and filtered through a 70 μm nylon mesh. Isolated cells were then further purified with a Percoll gradient (GE Healthcare). Fetal liver and spleen tissues were cut into small pieces and filtered through a 70 μm nylon cell strainer and the immune cells were isolated with Ficoll-Paque™ density gradient (provided by apothecary LUMC). All the isolated cells were stored in liquid nitrogen. Study approval was granted by the Medical Ethics Commission of Leiden University Medical Centre (protocol P08.087). All experiments were conducted in accordance with local ethical guidelines and the principles of the Declaration of Helsinki.

Cell suspension-mass cytometry

Antibodies used for cell suspension-mass cytometry are listed in Supplementary Table 1. Purified antibodies lacking carrier protein were conjugated with metal reporters by using a MaxPar X8 Antibody Labeling Kit (Fluidigm). Procedures for antibody staining and data acquisition were described previously[41]. Briefly, cells from fetal intestines were incubated with 5 μM Cell-ID Intercalator-103Rh (Fluidigm) for 15 min at rT and then stained with a cocktail of metal-conjugated antibodies for 45 min at rT. After washing, cells were incubated with 125 nM Cell-ID Intercalator-Ir (Fluidigm) in MaxPar Fix and Perm Buffer (Fluidigm) overnight at 4 °C. Data were acquired using a CyTOF 2™ mass cytometer (Fluidigm) and normalized using EQ Four Element Calibration Beads with the reference EQ Passport P13H2302 (Fluidigm).

Imaging-mass cytometry

Antibodies used for imaging-mass cytometry are listed in Supplementary Table 3. Purified antibodies lacking carrier protein were conjugated with metal reporters by using a MaxPar X8 Antibody Labeling Kit (Fluidigm). Snap-frozen human fetal intestinal biopsies were sectioned at a thickness of 5 μm and fixed by incubating with 1% paraformaldehyde for 5 min at rT followed by 100% methanol for 5 min at –20 °C. After fixation, tissue sections were washed in Dulbecco's phosphate-buffered saline (Thermo Fisher Scientific) containing 0.5% bovine serum albumin and 0.05% Tween, rehydrated in additive-free Dulbecco's phosphate-buffered saline, washed again, and blocked with Superblock Solution (Thermo Fisher Scientific). Tissue sections were then stained with a cocktail of metal-conjugated antibodies overnight at 4 °C, washed, and incubated with 125 nM Cell-ID Intercalator-Ir for 30 min at rT. After a further wash, tissue sections were dipped in Milli-Q water (Merck Millipore) for 1 min and dried for 20 min at rT. Data were acquired using a Hyperion™ imaging-mass cytometer (Fluidigm) at a resolution of 1 μm, with settings aligned to company guidelines. The ablation frequency was 200 Hz, and the energy was 6 dB. Regions of interest were acquired at a size of 1 by 1 mm^2. All data were stored as MCD files and txt files.

Single-cell RNA-sequencing

Single, live, CD8a$^-$TCRγδ$^-$CD4$^+$ cells from the intestines of fetus #6 were sorted using a FACSAria III flow cytometer (BD Biosciences). Post-sort purity was 96.5%. Single-cell RNA-sequencing was performed as described previously[42]. Briefly, cells combined with oil, reagents, and beads were loaded on a Chromium Single Cell Controller (10x Genomics). Lysis and barcoded reverse transcription of polyadenylated mRNA from single cells were performed inside each gel bead emulsion. Next-generation sequencing libraries were prepared in a single bulk reaction, and transcripts were sequenced using a HiSeq4000 System (Illumina).

Integrated data analysis

For cell suspension-mass cytometry, data from single, live, CD45$^+$ cells, gated individually using Cytobank as shown in Supplementary Fig. 1a, were sample-tagged and hyperbolic-arcsinh-transformed with a cofactor of 5 using Cytosplore^{+HSNE} software[13]. The major immune lineages shown in Supplementary Fig. 1b were then identified at the overview level by performing a 3-level HSNE analysis carried out with default parameters (perplexity: 30; iterations: 1,000). All t-SNE plots and Gaussian Mean-Shift clustering-derived cell clusters were generated in Cytosplore[15]. Hierarchical clustering of the phenotype heatmap was created with Euclidean correction and average linkage clustering in Cytosplore^{+HSNE}. Violin plots for cytometry data were generated in R. Diffusion map plots for mass cytometry data were generated using the "density" package in R. Single-cell force-directed layouts for mass cytometry data were generated using "VorteX" software[19]. For imaging-mass cytometry, all images were generated using MCD Viewer software v1.0.560 (Fluidigm). For single-cell RNA-seq, single-cell transcriptome sequencing data were processed using the single-cell RNA-seq package "Seurat" in R[16]. The Seurat object was generated by following the criteria that each gene was expressed by at least 3 cells and that at least 200 genes were

expressed per cell. Data were further filtered based on the parameters: (i) unique gene count per cell >200 and <2,000; and (ii) mitochondrial percentage of all genes <0.05. After log-normalization, a PCA-reduction analysis (pcs.compute = 20) was performed based on the 2,174 variable genes across single cells. Next, graph-based clustering detection and a t-SNE algorithm were applied to the top 13 PCA-dimensions. The resolution for cluster detection was 0.8. Heatmaps, PCA plots, diffusion map plots, and violin plots of the RNA-seq data were generated using the "Seurat" package. The t-SNE plots for RNA-seq data shown in Fig. 4b were generated in Cytosplore[+HSNE]. Only genes with local standardization (>0.5) across all cells were taken into account. Bar graphs and dot plots (showing mean and SD) were generated in Prism (GraphPad). The pseudotime analysis shown in Fig. 4c,d was performed using the Monocle 2 toolkit in R as described previously[22], excluding unrelated T_{reg} cells. Briefly, the single-cell trajectory was inferred using the dpFeature unsupervised procedure to identify variable genes, and the dimensions were reduced using t-SNE on the top high-loading principal components. The top 1,000 significant genes were selected as the ordering genes and reduced with the DDRTree method for the single-cell graph shown in Fig. 4c. Variable genes were selected at a significant false discovery rate of <10%, clustered by pseudo-temporal expression patterns, and visualized in a heatmap in Fig. 4d. Gene list enrichment analysis was performed using ToppGene[43], gene interaction network analysis was performed using the BioGrid interaction database[44], and gene pathway analysis was performed using the Kyoto Encyclopedia of Genes and Genomes[45].

Flow cytometry

For surface staining, cells were incubated with fluorochrome-conjugated antibodies and human Fc block (BioLegend) for 30–45 min at 4 °C. For intracellular cytokine/CD154 staining, cells were stimulated with CD3/CD28-specific (2.5 μg/mL each, BioLegend) or control antibodies (5 μg/mL, BioLegend) for 4 h at 37 °C. Brefeldin A (10 μg/mL, Sigma) was added for the final 3 h. Cells were then fixed/permeabilized using Fixation Buffer and Intracellular Staining Perm Wash Buffer (BioLegend). For intracellular Foxp3/Ki-67 staining, cells were prepared using a Foxp3 Staining Buffer Set (eBioscience). Electronic compensation was performed using individually stained CompBeads (BD Biosciences). Cells were acquired using an LSR II cytometer (BD Biosciences) or sorted using a FACSAria III flow cytometer (BD Biosciences) as shown in Supplementary Fig. 3a. Data were analyzed with FlowJo software v10 (Tree Star Inc.). The antibodies used in this study are listed in Supplementary Table 4.

TCR repertoire analysis

CD4^{+} T cell subsets were sorted according to the gating strategy shown in Supplementary Fig. 3a. For conventional sequencing, a total of 5,000 cells per subset was sorted directly into RNAlater (Applied Biosystems) using a FACSAria III flow cytometer (BD Biosciences). All expressed TCRβ rearrangements were amplified using a template-switch anchored RT-PCR, sequenced, and analyzed as described previously[46]. Gene use was determined according to the ImMunoGeneTics (IMGT) nomenclature[47].

For high-throughput sequencing, an average of 6,700 ± 2,000 cells per subset was sorted directly into RLT buffer (Qiagen) using a FACSAria III flow cytometer (BD Biosciences).

Four volumes of TRIzol (Invitrogen) were then added to the RLT cell lysate. RNA was extracted according to the TRIzol Reagent User Guide. Unique molecular identifier (UMI)-labelled 5'RACE TCRα and TCRβ cDNA libraries were prepared using a Human TCR Profiling Kit (MiLaboratory LLC). All extracted RNA was used for cDNA synthesis, and all synthesized cDNA was used for PCR amplification. Libraries were prepared in parallel using the same number of PCR cycles and sequenced in parallel using a 150 + 150 bp MiSeq System (Illumina). This approach generated a total of 11,310,000 TCRα and TCRβ sequencing reads (250,000 ± 150,000 reads per library), from which 625,000 unique unique UMI-labelled TCR cDNA molecules (13,500 ± 7,000 molecules per library) were extracted using MIGEC48 and MiXCR49 software with a threshold of at least 2 sequencing reads per UMI. Each library contained an average of 3,500 ± 1,300 functional (in-frame, without stop-codons) CDR3 nucleotide sequences. Averaged TCR repertoire characteristics weighted by clonotype size were analyzed using VDJtools software27. Gene use was determined according to the ImMunoGeneTics (IMGT) nomenclature47.

Statistics

Results are shown as mean ± SEM. The statistics test used were two-tailed Wilcoxon matched-pairs signed-ranks test and Kruskal-Wallis test with Dunn's test for multiple group comparisons, as appropriate (after normality test). P   0.05 was considered to be statistically significant. All statistics were analysed using GraphPad Prism 7 software.

Supplementary Material

Refer to Web version on PubMed Central for supplementary material.

Acknowledgments

References

1. Janeway CA Jr. Approaching the asymptote? Evolution and revolution in immunology. Cold Spring Harb Symp Quant Biol. 1989; 54(Pt 1):1–13.

2. Fan X, Rudensky AY. Hallmarks of Tissue-Resident Lymphocytes. Cell. 2016; 164:1198–1211. [PubMed: 26967286]

3. Thome JJC, et al. Early-life compartmentalization of human T cell differentiation and regulatory function in mucosal and lymphoid tissues. Nat Med. 2015; 22:72–77. [PubMed: 26657141]

4. Bunders MJ, et al. Memory CD4(+)CCR5(+) T cells are abundantly present in the gut of newborn infants to facilitate mother-to-child transmission of HIV-1. Blood. 2012; 120:4383–4390. [PubMed: 23033270]

5. Zhang X, et al. CD4 T cells with effector memory phenotype and function develop in the sterile environment of the fetus. Sci Transl Med. 2014; 6:238ra72.

6. Stout MJ, et al. Identification of intracellular bacteria in the basal plate of the human placenta in term and preterm gestations. Am J Obstet Gynecol. 2013; 208:226.e1–7. [PubMed: 23333552]

7. Aagaard K, et al. The placenta harbors a unique microbiome. Sci Transl Med. 2014; 6:237ra65.

8. Collado MC, Rautava S, Aakko J, Isolauri E, Salminen S. Human gut colonisation may be initiated in utero by distinct microbial communities in the placenta and amniotic fluid. Sci Rep. 2016; 6:23129. [PubMed: 27001291]

9. DiGiulio DB. Diversity of microbes in amniotic fluid. Semin Fetal Neonatal Med. 2012; 17:2–11. [PubMed: 22137615]

10. Ardissone AN, et al. Meconium microbiome analysis identifies bacteria correlated with premature birth. PLoS One. 2014; 9:e90784. [PubMed: 24614698]

11. Hornef M, Penders J. Does a prenatal bacterial microbiota exist? Mucosal Immunol. 2017; 10:598–601. [PubMed: 28120852]

12. Li N, et al. Mass cytometry reveals innate lymphoid cell differentiation pathways in the human fetal intestine. J Exp Med. 2018; 215:1383–1396. [PubMed: 29511064]

13. van Unen V, et al. Visual analysis of mass cytometry data by hierarchical stochastic neighbour embedding reveals rare cell types. Nat Commun. 2017; 8:1740. [PubMed: 29170529]

14. van der Maaten L, Hinton G. Visualizing Data using t-SNE. J Mach Learn Res. 2008; 9:2579–2605.

15. Höllt T, et al. Cytosplore: Interactive Immune Cell Phenotyping for Large Single-Cell Datasets. Comput Graph Forum. 2016; 35:171–180.

16. Butler A, Hoffman P, Smibert P, Papalexi E, Satija R. Integrating single-cell transcriptomic data across different conditions, technologies, and species. Nat Biotechnol. 2018; 36:411–420. [PubMed: 29608179]

17. Kimmig S, et al. Two subsets of naive T helper cells with distinct T cell receptor excision circle content in human adult peripheral blood. J Exp Med. 2002; 195:789–794. [PubMed: 11901204]

18. Angerer P, et al. destiny – diffusion maps for large-scale single-cell data in R. Bioinformatics. 2015; 32:1241–1243. [PubMed: 26668002]

19. Samusik N, Good Z, Spitzer MH, Davis KL, Nolan GP. Automated mapping of phenotype space with single-cell data. Nat Methods. 2016; 13:493–496. [PubMed: 27183440]

20. Jolliffe, I. Principal Component AnalysisInternational Encyclopedia of Statistical Science. 2011. 1094–1096.

21. Trapnell C, et al. The dynamics and regulators of cell fate decisions are revealed by pseudotemporal ordering of single cells. Nat Biotechnol. 2014; 32:381–386. [PubMed: 24658644]

22. Qiu X, et al. Single-cell mRNA quantification and differential analysis with Census. Nat Methods. 2017; 14:309–315. [PubMed: 28114287]

23. Azzam HS, et al. CD5 Expression Is Developmentally Regulated By T Cell Receptor (TCR) Signals and TCR Avidity. J Exp Med. 1998; 188:2301–2311. [PubMed: 9858516]

24. Mandl JN, Monteiro JP, Vrisekoop N, Germain RN. T Cell-Positive Selection Uses Self-Ligand Binding Strength to Optimize Repertoire Recognition of Foreign Antigens. Immunity. 2013; 38:263–274. [PubMed: 23290521]

25. Persaud SP, Parker CR, Lo W-L, Scott Weber K, Allen PM. Intrinsic CD4 T cell sensitivity and response to a pathogen are set and sustained by avidity for thymic and peripheral complexes of self peptide and MHC. Nat Immunol. 2014; 15:266–274. [PubMed: 24487322]

26. Fulton RB, et al. The TCR's sensitivity to self peptide-MHC dictates the ability of naive CD8(+) T cells to respond to foreign antigens. Nat Immunol. 2015; 16:107–117. [PubMed: 25419629]

27. Shugay M, et al. VDJtools: Unifying Post-analysis of T Cell Receptor Repertoires. PLoS Comput Biol. 2015; 11:e1004503. [PubMed: 26606115]

28. Egorov ES, et al. The Changing Landscape of Naive T Cell Receptor Repertoire With Human Aging. Front Immunol. 2018; 9:1618. [PubMed: 30087674]

29. Miyazawa S, Jernigan RL. Residue-residue potentials with a favorable contact pair term and an unfavorable high packing density term, for simulation and threading. J Mol Biol. 1996; 256:623–644. [PubMed: 8604144]

30. Kidera A, Konishi Y, Oka M, Ooi T, Scheraga HA. Statistical analysis of the physical properties of the 20 naturally occurring amino acids. J Protein Chem. 1985; 4:23–55.

31. Rackovsky S. Global characteristics of protein sequences and their implications. Proc Natl Acad Sci U S A. 2010; 107:8623–8626. [PubMed: 20421501]

32. Pezzotti N, et al. Approximated and User Steerable tSNE for Progressive Visual Analytics. IEEE Trans Vis Comput Graph. 2017; 23:1739–1752. [PubMed: 28113434]

33. Fergusson JR, et al. CD161 defines a transcriptional and functional phenotype across distinct human T cell lineages. Cell Rep. 2014; 9:1075–1088. [PubMed: 25437561]

34. Edfors F, et al. Gene-specific correlation of RNA and protein levels in human cells and tissues. Mol Syst Biol. 2016; 12:883. [PubMed: 27951527]

35. McFarland RD, Douek DC, Koup RA, Picker LJ. Identification of a human recent thymic emigrant phenotype. Proc Natl Acad Sci U S A. 2000; 97:4215–4220. [PubMed: 10737767]

36. Staton TL, et al. CD8+ recent thymic emigrants home to and efficiently repopulate the small intestine epithelium. Nat Immunol. 2006; 7:482–488. [PubMed: 16582913]

37. Michaelsson J, Mold JE, McCune JM, Nixon DF. Regulation of T Cell Responses in the Developing Human Fetus. The Journal of Immunology. 2006; 176:5741–5748. [PubMed: 16670279]

38. Feng Y, et al. A mechanism for expansion of regulatory T-cell repertoire and its role in self-tolerance. Nature. 2015; 528:132–136. [PubMed: 26605529]

39. Allenspach EJ, et al. Absence of functional fetal regulatory T cells in humans causes in utero organ-specific autoimmunity. J Allergy Clin Immunol. 2017; 140:616–619.e7. [PubMed: 28322850]

40. Gomez de Agüero M, et al. The maternal microbiota drives early postnatal innate immune development. Science. 2016; 351:1296–1302. [PubMed: 26989247]

41. van Unen V, et al. Mass Cytometry of the Human Mucosal Immune System Identifies Tissue- and Disease-Associated Immune Subsets. Immunity. 2016; 44:1227–1239. [PubMed: 27178470]

42. Zheng GXY, et al. Massively parallel digital transcriptional profiling of single cells. Nat Commun. 2017; 8:14049. [PubMed: 28091601]

43. Chen J, Bardes EE, Aronow BJ, Jegga AG. ToppGene Suite for gene list enrichment analysis and candidate gene prioritization. Nucleic Acids Res. 2009; 37:W305–W311. [PubMed: 19465376]

44. Bean DM, et al. esyN: network building, sharing and publishing. PLoS One. 2014; 9:e106035. [PubMed: 25181461]

45. Ogata H, et al. KEGG: Kyoto Encyclopedia of Genes and Genomes. Nucleic Acids Res. 1999; 27:29–34. [PubMed: 9847135]

46. Quigley MF, Almeida JR, Price DA, Douek DC. Unbiased molecular analysis of T cell receptor expression using template-switch anchored RT-PCR. Curr Protoc Immunol. 2011; Chapter 10:Unit10.33.

47. Lefranc M-P, et al. IMGT unique numbering for immunoglobulin and T cell receptor constant domains and Ig superfamily C-like domains. Dev Comp Immunol. 2005; 29:185–203. [PubMed: 15572068]

48. Shugay M, et al. Towards error-free profiling of immune repertoires. Nat Methods. 2014; 11:653–655. [PubMed: 24793455]

49. Bolotin DA, et al. MiXCR: software for comprehensive adaptive immunity profiling. Nat Methods. 2015; 12:380–381. [PubMed: 25924071]
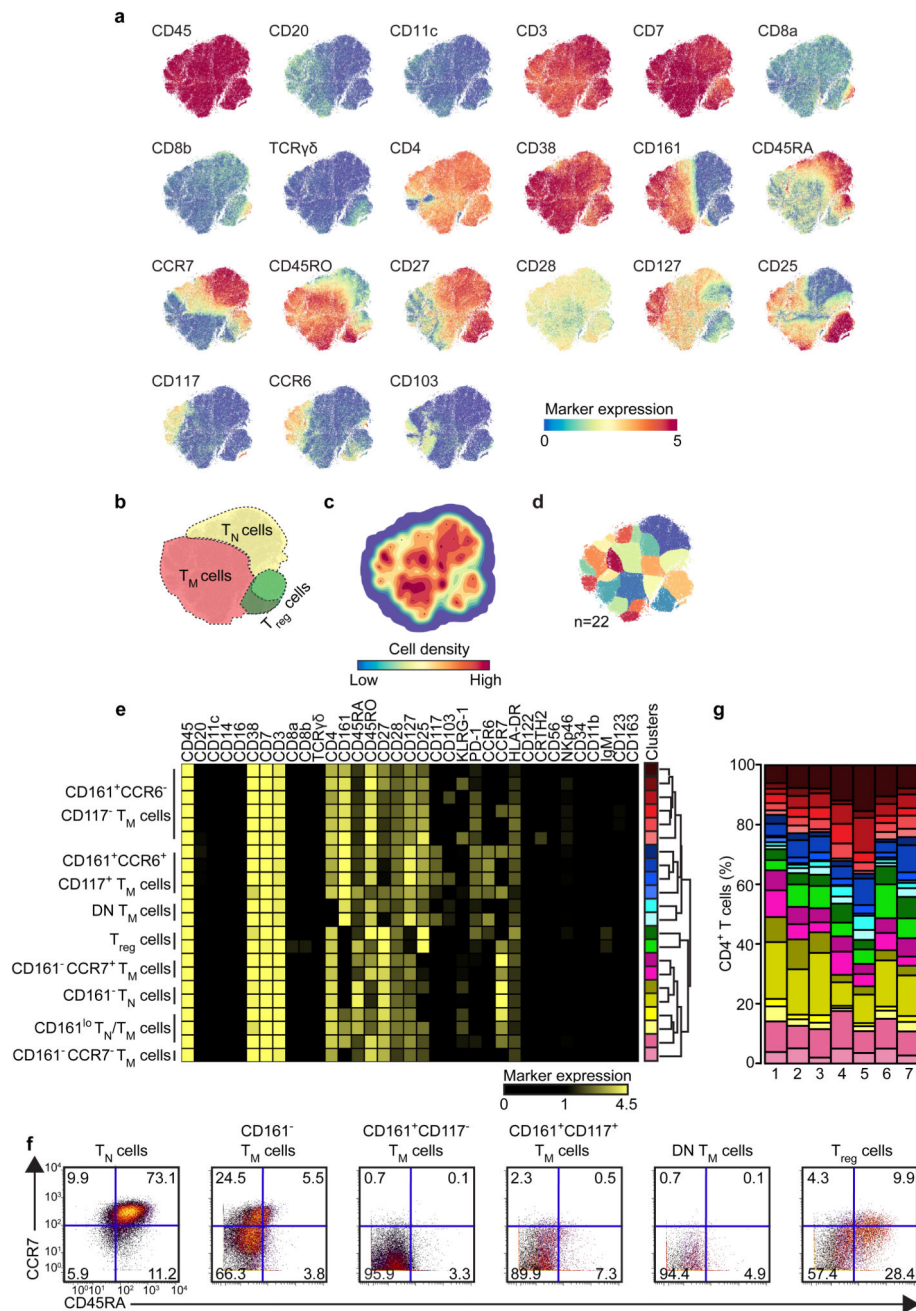
Fig. 1. Mass cytometric analysis of fetal intestinal CD4$^+$ T cells.

a, t-SNE embedding of all CD4$^+$ T cells (n = 110,332) derived from human fetal intestines (n = 7). Colors represent the ArcSinh5-transformed expression values of the indicated markers. **b**, t-SNE plot depicting the population cell border for T$_N$ cells (dashed yellow line), T$_M$ cells (dashed red line), and T$_{reg}$ cells (dashed green line). **c**, Density map describing the local probability density of cells, where black dots indicate the centroids of identified clusters using Gaussian mean-shift clustering. **d**, t-SNE plot showing cluster partitions in different colors. **e**, Heatmap showing median expression values and hierarchical clustering

of markers for the identified subpopulations. **f**, Biaxial plots showing CD45RA and CCR7 expression on the indicated clusters analyzed by mass cytometry. The 22 clusters were merged into 6 phenotypic groups according to the heatmap shown in (**e**). **g**, Composition of the CD4$^+$ T cell compartment in each fetal intestine represented by vertical bars, where the colored segment lengths represent the proportion of cells as a percentage of all CD4$^+$ T cells in the sample. Colors as shown in (**e**).
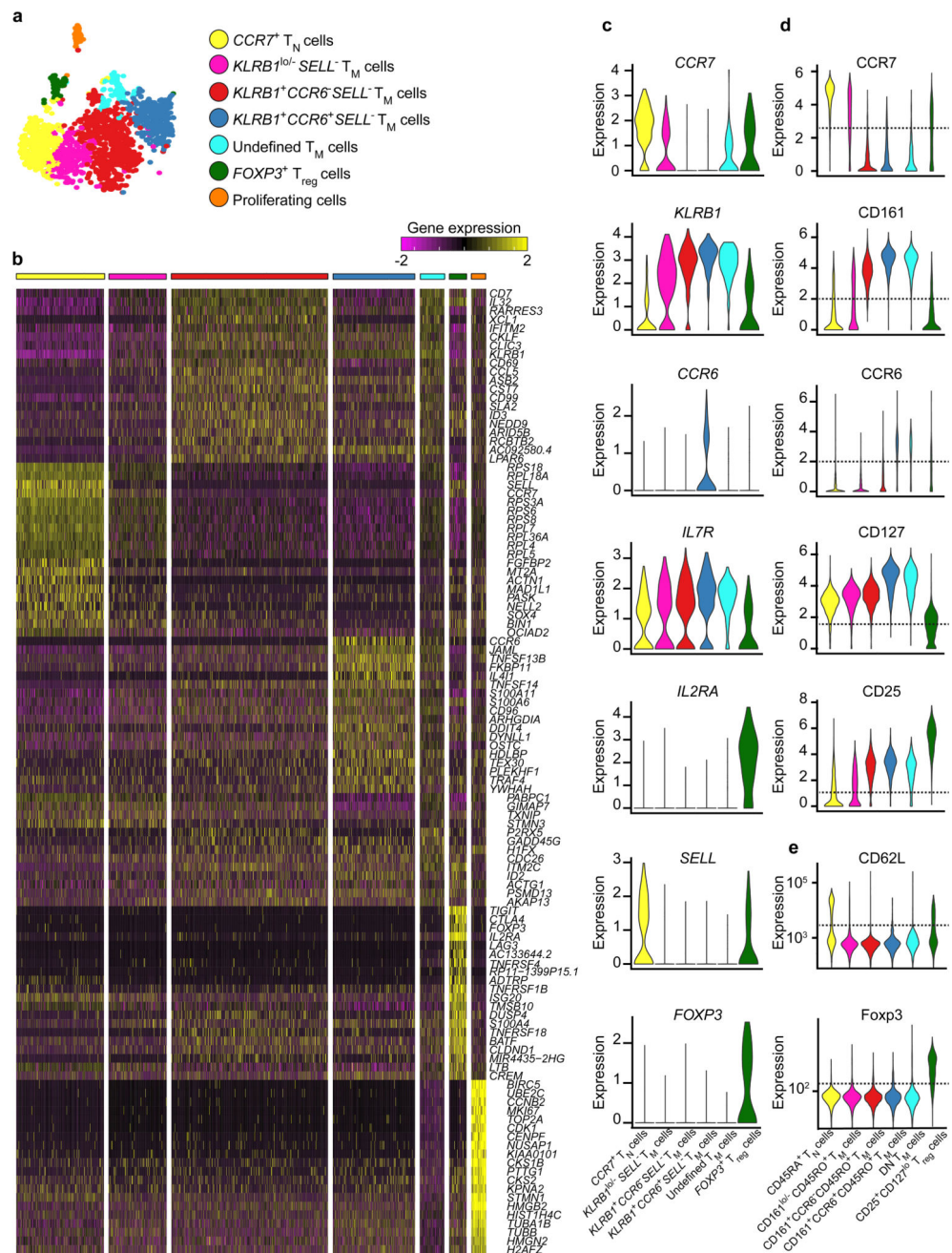
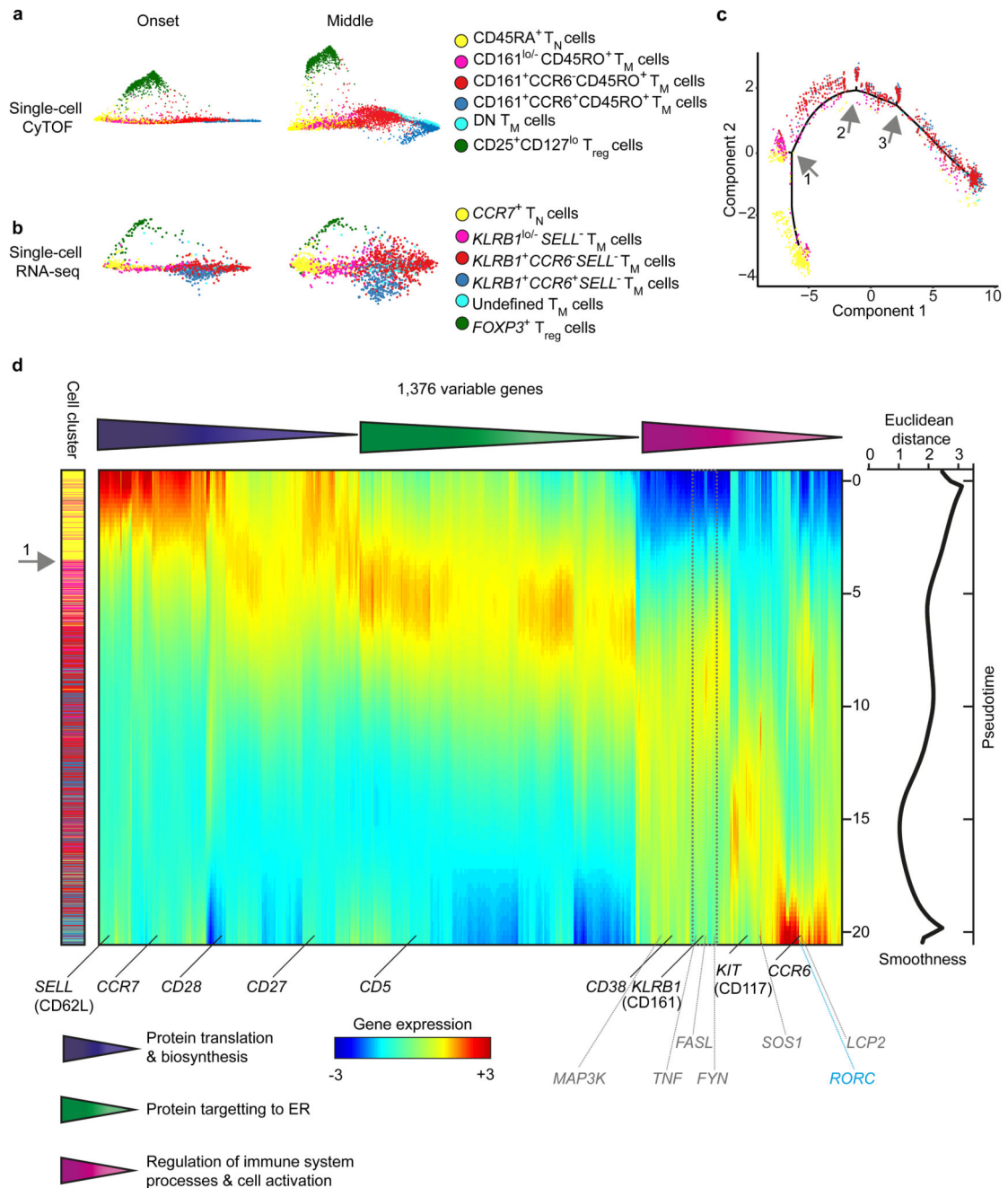**Fig. 2. Single-cell RNA-sequencing of fetal intestinal CD4$^+$ T cells.**

a, t-SNE embedding of fetal intestinal CD4$^+$ T cells (n = 1,804) showing seven transcriptionally distinct clusters, including *CCR7*$^+$ T$_N$ (n = 358), *KLRB1*$^{lo/-}$*SELL*$^-$ T$_M$ (n = 237), *KLRB1*$^+$*CCR6*$^-$*SELL*$^-$ T$_M$ (n = 640), *KLRB1*$^+$*CCR6*$^+$*SELL*$^-$ T$_M$ (n = 336), undefined T$_M$ (n = 101), *FOXP3*$^+$ T$_{reg}$ cells (n = 71), and proliferating cells (n =61). Colors indicate different cell clusters. **b**, Heatmap showing the normalized single-cell gene expression value (Z-Score, purple-to-yellow scale) for the top 20 differentially upregulated genes in each identified cluster. Colors as shown in (**a**). **c–e**, Expression of the indicated genes in each

identified cluster at (**c**) the RNA level (log-normalized) and (**d,e**) the protein level analyzed by (**d**) mass cytometry (CyTOF, ArcSinh5-transformed) or (**e**) flow cytometry, presented as violin plots. Dashed lines indicate background levels. Colors as shown in (**a**).
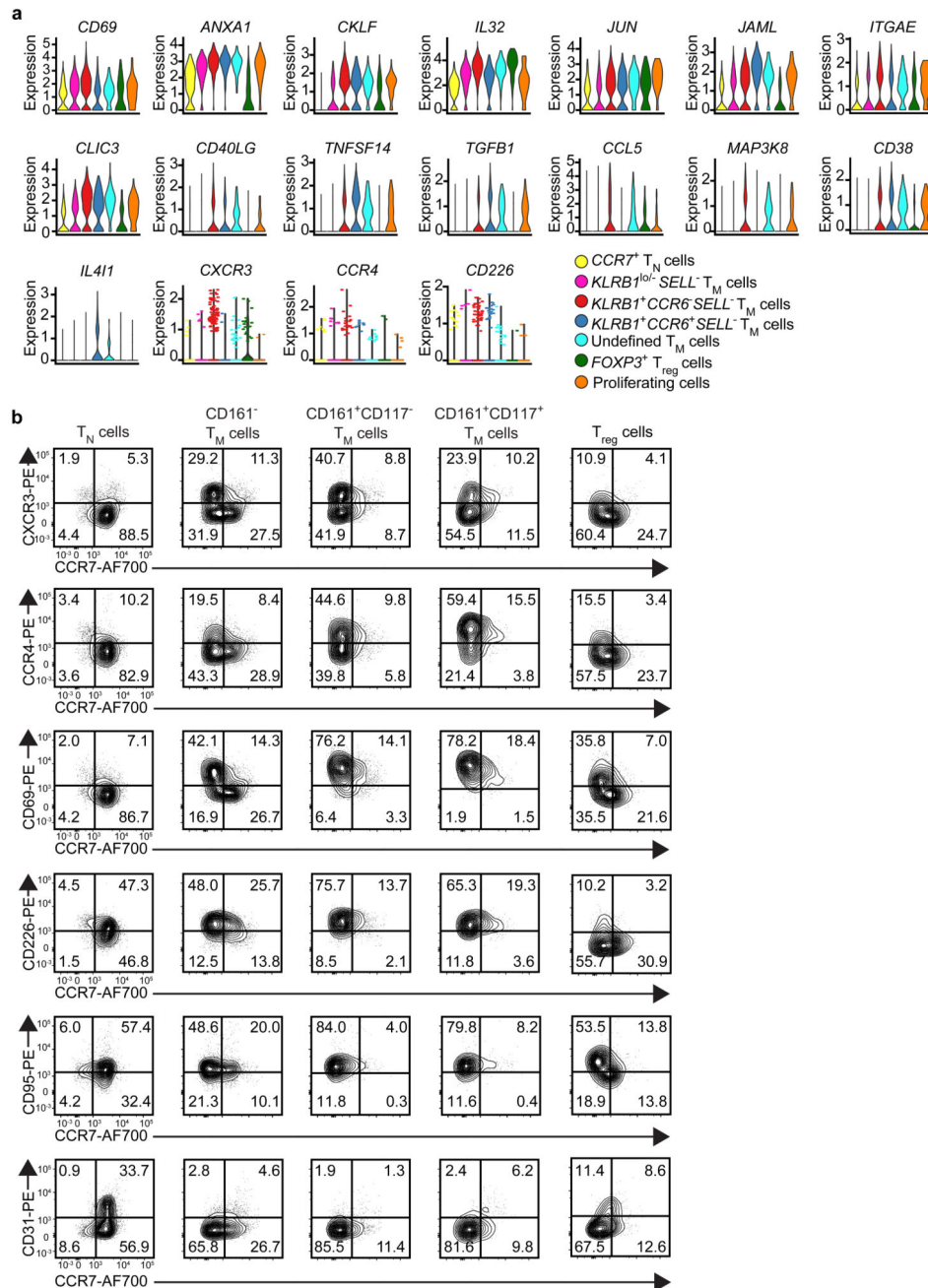
**Fig. 3. Targeted analysis of memory-like fetal intestinal CD4+ T cells.**
a, Expression (log-normalized) of the indicated genes in distinct CD4+ T cell clusters as determined by single-cell RNA-seq analysis, presented as violin plots. Colors indicate different cell clusters. **b**, Biaxial plots showing expression of CXCR3, CCR4, CD69, CD226, CD95, and CD31 vs. CCR7 on the indicated CD4+ T cell clusters analyzed by flow cytometry. Data represent two to three independent experiments.

Fig. 4. Single-cell trajectory analysis of fetal intestinal CD4+ T cells.
a–b, t-SNE embeddings of all fetal intestinal CD4+ T cells analyzed by (**a**) mass cytometry (n = 10,436) and (**b**) single-cell RNA-seq (n = 1,743) at the onset and at the middle of the t-SNE computation. Colors indicate different cell clusters. **c**, A single-cell trajectory from the RNA-seq data (excluding T_{reg} cells and proliferating cells) recovered by pseudotime analysis. Colors indicate different cell clusters as shown in (**b**). Grey arrows indicate three small branches. **d**, Three kinetic modules of pseudotime-dependent genes (n = 1,376) depicted in a log-variance-stabilized expression heatmap, indicating gene-enriched

biological processes. Genes confirmed by mass cytometry and flow cytometry are denoted by black labels, and genes involved in TCR signalling are denoted by gray labels. The dashed grey box indicates the coordinated expression profile of TNF, FASL, and FYN. Euclidean distance values comparing gene expression profiles for each ordered pair of neighboring cells along the pseudotime trajectory are shown in the graph (right).
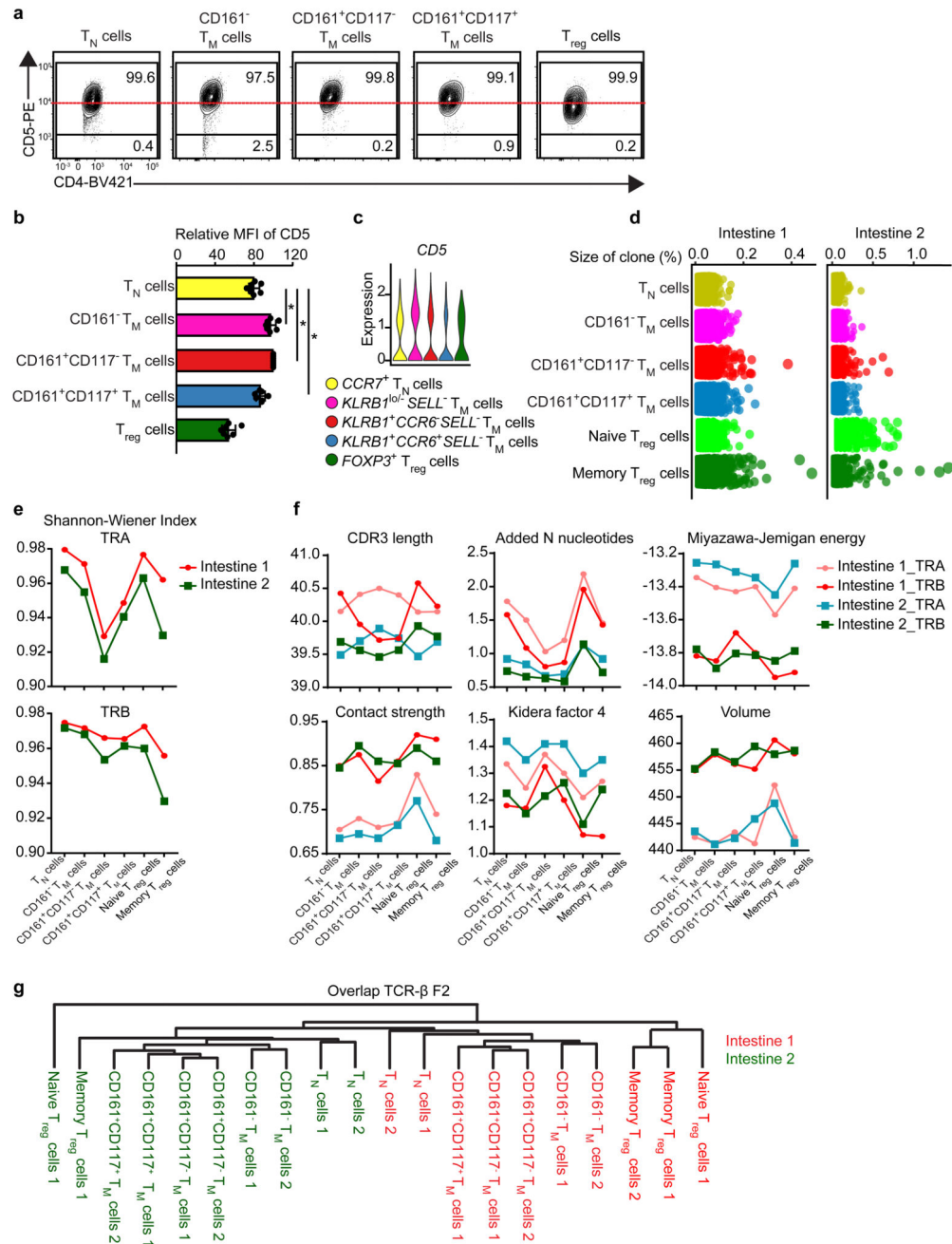
Fig. 5. CD5 expression analysis and high-throughput TCR-sequencing of fetal intestinal CD4$^+$ T cells.

a–b, CD5 expression on the indicated CD4$^+$ T cell clusters. (**a**) The biaxial plots depict one representative experiment, and (**b**) the bar graphs depict the median fluorescence intensity (MFI) of CD5 expression for each cluster relative to the corresponding CD161$^+$CD117$^-$ T$_M$ subpopulation in each fetal intestine (n = 7). Data represent six independent experiments. Error bars indicate mean ± SEM. *p < 0.05, Two-tailed Wilcoxon matched-pairs signed-ranks test. **c**, Expression (log-normalized) of *CD5* gene transcripts in the indicated cell

clusters, presented as violin plots. **d**, Dot plots showing the percentage of TCR cDNA molecules per unique TCRβ sequence in each cluster from each fetal intestine. Data are from two independent samples. A single duplicate is shown for samples with technical replicates. **e**, Dot plots showing the normalized Shannon-Wiener index for TCRα (TRA) and TCRβ (TRB) sequences in each cluster from each fetal intestine. Data are from two independent samples. **f**, Dot plots showing averaged TCR repertoire characteristics weighted per clonotype for each cluster. Data are from two independent samples. **g**, Dendrogram showing weighted clonal overlaps for TCRβ nucleotide sequences among clusters, analyzed using the F2 similarity metric in VDJtools. Colors indicate different fetal intestines.
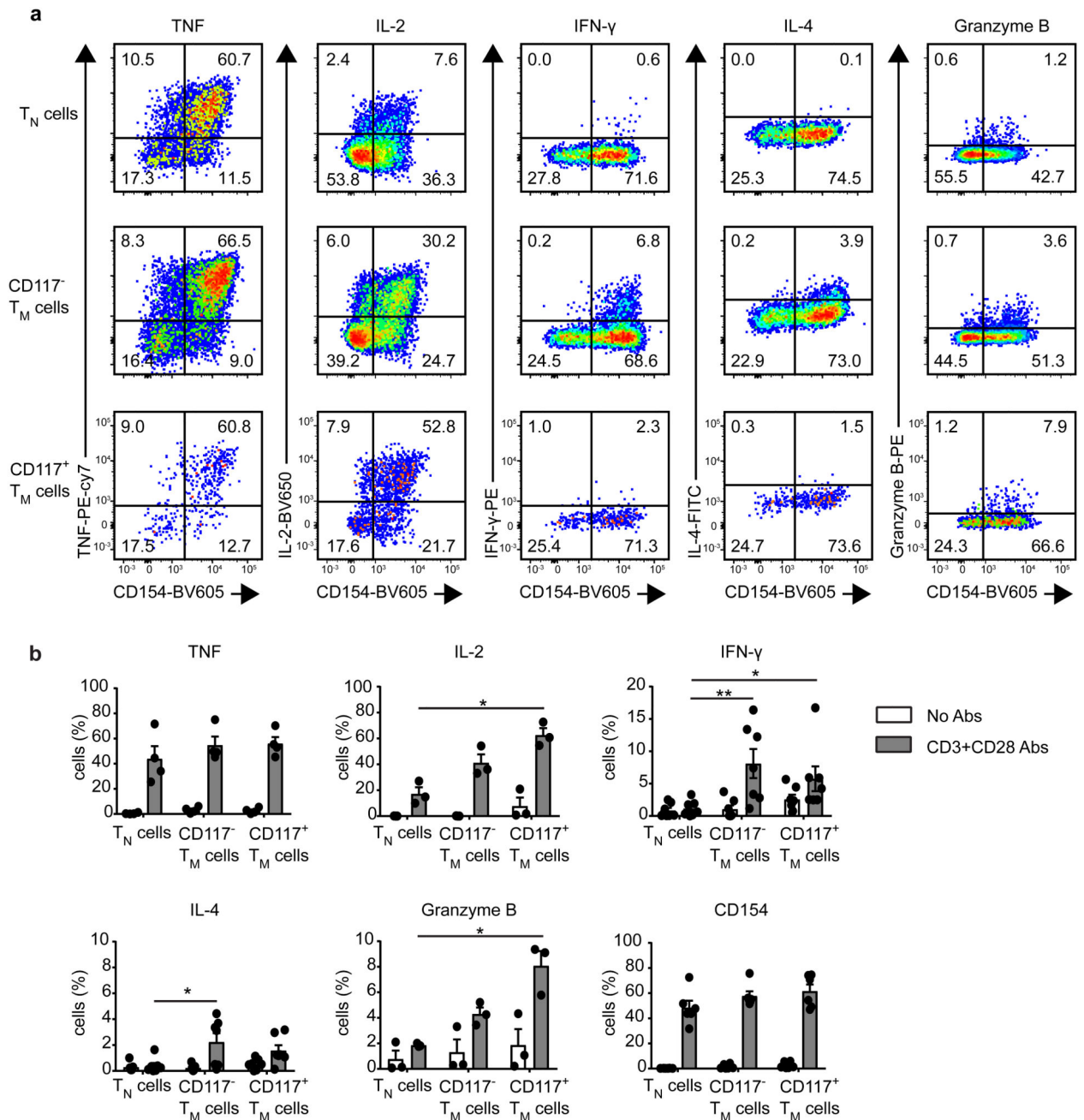
Fig. 6. Functional profiling of fetal intestinal CD4+ T cells.
a–b, Purified fetal intestinal CD4+ T cells were treated with a control antibody or stimulated with anti-CD3 and anti-CD28 for 4 h. Intracellular expression of TNF, IL-2, IFN-γ, IL-4, granzyme B, and CD154 was determined for each subpopulation by flow cytometry. (**a**) The biaxial plots show data from one representative experiment after stimulation with anti-CD3 and anti-CD28, and (**b**) the bar charts show data for each subpopulation from each fetal intestine (TNF: n = 4 samples in two independent experiments; IL-2 and granzyme B: n = 3 samples in two independent experiments; IFN-γ, IL-4 and CD154: n = 7 samples in four

independent experiments). Error bars indicate mean ± SEM. *p < 0.05, **p <0.01, Kruskal-Wallis test with Dunn's test for multiple comparisons.
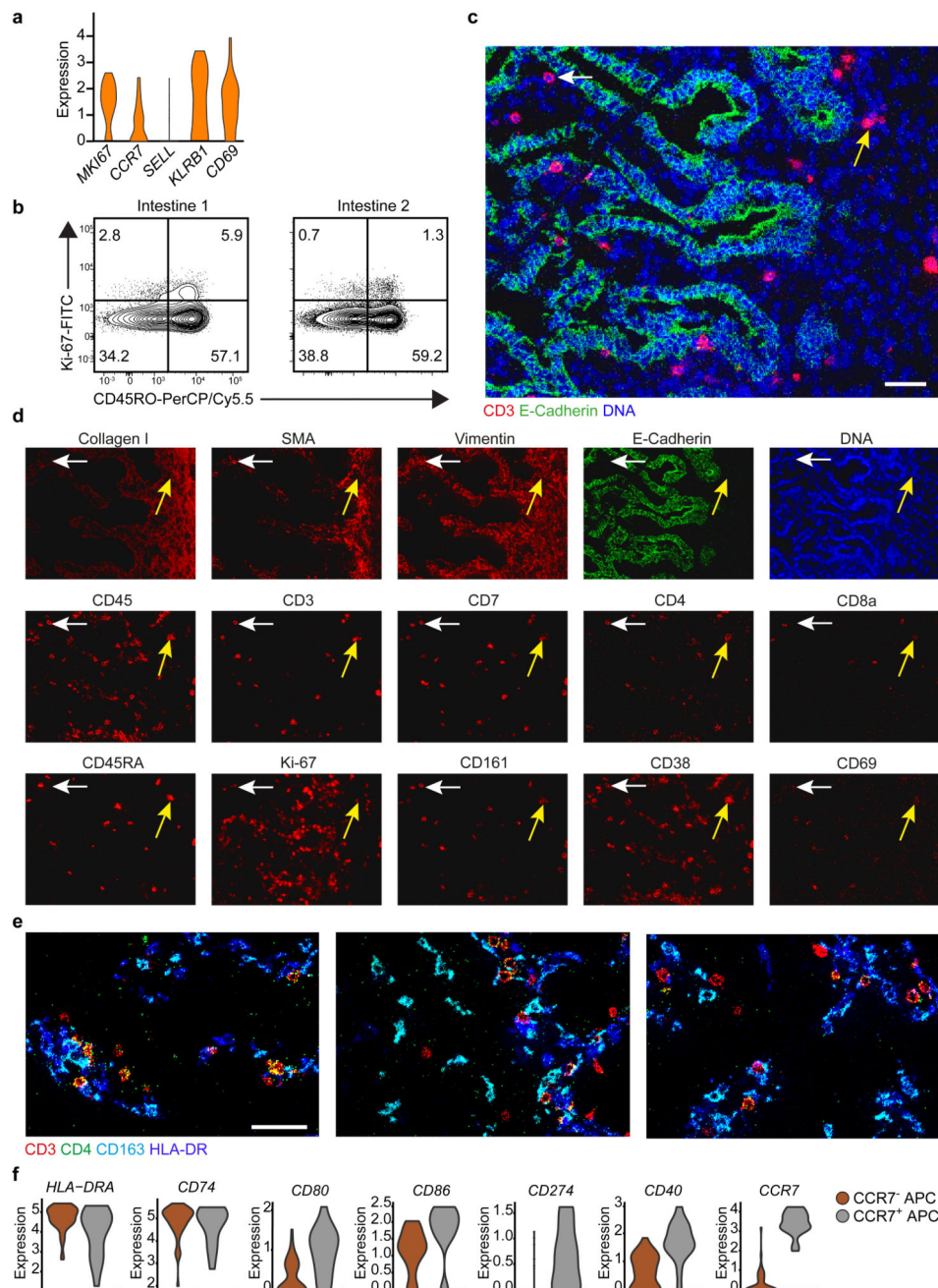
Fig. 7. Characterization and spatial localization of fetal intestinal CD4+ T cells and APCs.
a, Expression (log-normalized) of the indicated genes in proliferating fetal intestinal CD4+ T cells, presented as violin plot. **b**, Biaxial plots showing expression of Ki-67 vs. CD45RO in the fetal intestinal CD4+ T cell compartment analyzed by flow cytometry. Data represent two independent experiments. **c**, Representative mass cytometry image of a fetal intestine showing the overlay of CD3 (red), Ecadherin (green), and DNA (blue). Scale bar, 100 μm. **d**, Representative mass cytometry images of fetal intestines showing expression of the indicated stromal markers, immune markers, Ki-67 and DNA by the cells identified in (**c**).

Yellow arrows: $CD4^+CD45RA^+$ T_N cells; white arrows: $CD4^+CD45RA^-$ T_M cells. **e**, Representative mass cytometry images of a fetal intestine showing the overlay of CD3 (red), CD4(green), CD163 (cyan), and HLA-DR (blue). Scale bar, 50 μm. Colors and scale bars are similar in all three panels. Data in (**b-d**) represent four independent samples in four independent experiments. **f**, Expression (log-normalized) of the indicated genes in two clusters of APCs, presented as violin plots. $CCR7^-$ APCs (n = 49), $CCR7^+$ APCs (n = 17).